AC Loss Calculation and Analysis in Armature Windings for Superconducting Electrical Machines

Othman Taalibi and Tabea Arndt

***Abstract*—AC losses in armature windings arise from time-varying currents and fields, raising effective resistance and lowering efficiency. We compare three-phase armature winding losses for Litz wire and REBCO high-temperature superconductor (HTS) tapes, and examine how turn count and operating temperature affect them. For Litz windings, we use a hybrid analytical model that captures skin and proximity effects. For HTS windings, we develop a time-domain model that includes the angle and field-dependent critical current density $J_c(B, \theta)$ and power-law exponent $n(B, \theta)$. Both models are validated against finite-element method simulations. We then generate torque–speed loss maps under constraints from the drive and the cryocooler. The results provide a clear comparison of Litz and HTS armature windings across the entire operating speed range and offer recommendations for efficiency-oriented machine design and control.**

***Index Terms*—AC loss, armature windings, Litz wire, high temperature superconductor (HTS), torque–speed maps, finite element validation, cryocooler selection.**

I. Introduction

SUPERCONDUCTING electrical machines are strong candidates to replace conventional technologies in high-specific-power applications such as transportation and aviation [1], [2]. A major obstacle to their use is the armature-winding ac loss produced by time-varying currents and electromagnetic fields [3]. For windings made from normal-conductivity materials (e.g., copper or aluminum), these losses are mainly due to skin and proximity effects [4], [5], which increase the effective resistance as frequency increases; Litz conductors are commonly used to reduce these effects [6], but their benefit depends on material type, strand diameter, twist/transposition strategy [7], [8], and temperature-dependent conductivity [9], [10]. In contrast, high-temperature superconducting (HTS) REBCO tapes exhibit a nonlinear current–voltage characteristic, enabling high current density and negligible dc resistance. However, they incur magnetization (hysteresis) losses [11] that depend on the amplitudes of transport current and magnetic field, frequency, and the anisotropic properties $J_c(B, \theta)$ and $n(B, \theta)$ [12], as well as on how the critical current and the power-law index combine at the slot and phase levels through series and parallel connection paths.

Although simulation tools have advanced considerably, there is still no single, efficient framework that can generate operating maps comparing Litz and HTS armature windings over temperature, winding design (turn count, strand/tape size, number of parallel paths), drive limits, and cryocooler capabilities. This work addresses this gap using a hybrid modeling approach for armature-winding ac losses in partially and fully superconducting machines.

We develop a unified framework for evaluating armature-winding ac losses in electrical machines using either Litz conductors or REBCO HTS tapes. For Litz windings, we use a computationally efficient analytical model that combines classical skin- and proximity-effect formulations with turn- and bundle-level twist/transposition effects. For HTS windings, we implement a time-domain J-model [13], [14], [15] based on measured $J_c(B, \theta)$ and $n(B, \theta)$surfaces to compute instantaneous voltage and loss under arbitrary current and field waveforms. Both models are validated at the inductor level and at the machine level against finite-element simulations and measurements using JMAG [16] and COMSOL Multiphysics [17] over a range of temperatures, frequencies, and conductor configurations. Using the validated models, we compare winding materials and turn-count choices across operating temperature, then incorporate cryocooler performance limits through survey-based and datasheet-based models [18], [19], [20] to identify feasible operating points. Finally, we generate *d*–*q* and torque–speed loss maps under inverter and cryocooler constraints, enabling a region-by-region comparison of Litz and HTS armatures for efficiency-oriented machine design and control. The results reveal elliptical iso-loss contours in HTS designs and a reduced feasible torque–speed envelope relative to the Litz reference, with detailed analysis presented in Section V.

This article makes three main contributions. First, it provides a unified and computationally efficient framework for comparing Litz and HTS armature windings over temperature, winding design, and drive constraints. Second, it integrates a measurement-based time-domain J-model for REBCO tapes into machine-level analysis and validates it against finite-element results. Third, it incorporates cryocooler performance constraints directly into torque–speed loss maps, linking winding-loss physics to feasible operating regions and practical system-level design choices in superconducting electrical machines. The rest

Received 3 January 2026; revised 24 March 2026; accepted 14 April 2026. Date of publication 16 April 2026; date of current version 12 May 2026. This work was supported in part by the German Federal Ministry of Education and Research (BMBF) within the project TransHyDE, under Grant 03HY204A and in part by managed by the Project Management Agency Jülich (PTJ). *(Corresponding author: Othman Taalibi.)*

The authors are with the Institute of Technical Physics (ITEP), Karlsruhe Institute of Technology, 76344 Eggenstein-Leopoldshafen, Germany (e-mail: othman.taalibi@kit.edu; tabea.arndt@kit.edu).

Color versions of one or more figures in this article are available at https://doi.org/10.1109/TASC.2026.3684617.

Digital Object Identifier 10.1109/TASC.2026.3684617

© 2026 The Authors. This work is licensed under a Creative Commons Attribution 4.0 License. For more information, see https://creativecommons.org/licenses/by/4.0/

of this article is organized as follows. Section II reviews the armature-winding loss models and their assumptions. Section III describes the studied machine topology and the implementation of the Litz and HTS armatures. Section IV presents the comparative loss analysis versus material, turn count, and temperature, and discusses cryocooler selection. Section V presents the *d*–*q* and torque–speed loss maps and discusses the resulting operating-region trends. Section VI concludes this article.

II. ARMATURE WINDING LOSS MODELS

The electrical conductivity of armature-winding materials depends on both the conductor type and the operating temperature.

A. Materials With Linear (Ohmic) Conductivity: Stranded Conductors

In windings composed of stranded conductors made from materials with linear conductivity (e.g., Cu, Al), three types of ac losses can be identified [21]: skin-effect losses, which result from the tendency of current to concentrate near the conductor surface due to its self-field; proximity-effect losses, which arise from the redistribution of current caused by the magnetic field of adjacent conductors or by the rotating magnetic field of the rotor; and circulating-current losses, which occur due to local magnetic flux gradients between parallel strands, leading to unequal current distribution among the strands. The total ac loss can therefore be expressed as

$$P_{\text{AC}} = P_{\text{skin}} + P_{\text{proximity}} + P_{\text{circCurrent}}. \tag{1}$$

1) Skin Effect Losses: The increase in the effective resistance of a round conductor due to skin effect can be expressed by a coefficient K_{skin} derived from Maxwell's diffusion equation in the resistance-limited regime [4], for the case of sinusoidal current supply

$$K_{\text{skin}} = \frac{R_{\text{skin}}}{R_{\text{DC}}}. \tag{2}$$

For a round conductor, K_{skin} is [4]

$$K_{\text{skin}} = \frac{\gamma}{2} \cdot \frac{\text{ber}_0\left(\gamma\right)\text{bei}_0{}'\left(\gamma\right) - \text{bei}_0\left(\gamma\right)\text{ber}_0{}'\left(\gamma\right)}{\text{ber}_0{}'^2\left(\gamma\right) + \text{bei}_0{}'^2\left(\gamma\right)} \tag{3}$$

where $\text{ber}_0, \text{bei}_0$ are the order-0 Kelvin functions (real and imaginary parts, respectively) and primes denote derivatives with respect to γ.

The dimensionless parameter γ is [4]

$$\gamma = \frac{d_c}{\sqrt{2}\delta} \tag{4}$$

where d_c the conductor diameters, δ is the skin depth $\delta = \frac{1}{\sqrt{\pi f \mu_0 \sigma}}$ and σ_c is the conductor electrical conductivity.

The dc resistance of a single conductor with a cross-sectional area S_c and length L_c is

$$R_{\text{DC}} = \frac{L_c}{\sigma_c S_c}. \tag{5}$$

The corresponding average skin-effect losses for a sinusoidal current of peak amplitude I_{max} is

$$P_{\text{skin}} = \frac{I_{\text{max}}^2}{2} R_{\text{skin}} = I_{\text{rms}}^2 R_{\text{skin}}. \tag{6}$$

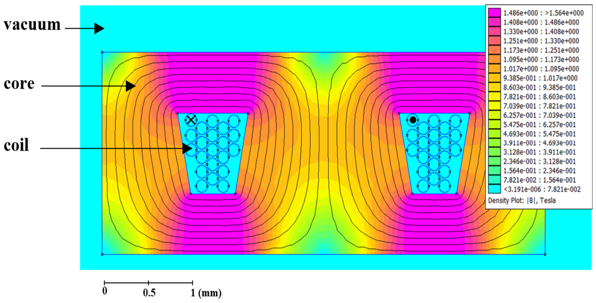

Fig. 1. Inductor configuration used for strands model validation, showing the magnetic flux density distribution for a strand diameter of 0.15 mm.

2) Proximity Effect Losses: A spatially uniform external sinusoidal magnetic flux density applied to a long round conductor induces eddy currents that dissipate power. In the classical (resistance-limited, $d_c \ll \delta$) regime, the average eddy-current (proximity) loss is [5]

$$P_{\text{proximity}} = \frac{\pi \sigma_c L_c d_c^4 \omega^2 B_{\text{max}}^2}{128}. \tag{7}$$

Here, $\omega = 2\pi f$ is the angular frequency (rad/s), f is the field frequency (Hz) and B_{max} is the maximum magnetic flux density (T).

3) Assumptions and Limitations:

1) Equations (1), (3), and (7) are derived for sinusoidal current excitation.
2) For nonsinusoidal excitation, the total loss is obtained by superposing the contributions of each harmonic from the Fourier decomposition of the current or the magnetic field, for both skin and proximity effects [22].
3) The orthogonality of loss components in (1) is valid only under uniform magnetic flux density B [23].
4) A uniform flux distribution is ensured when the conductor diameter is small compared with the spatial variation of the external magnetic field.
5) The analysis assumes a resistance-limited regime, which requires $d_c \ll \delta$. For practical use, a diameter limit $d_{\text{lim}} = 2\delta$ is adopted, and the model is applied only when $d_c < d_{\text{lim}}$.
6) Equation (7) retains only the dominant axial eddy-current component (current flowing along the conductor axis) induced by the transverse field.
7) Circulating current losses are neglected, assuming proper conductor twisting (360° full transposition) sufficiently reduces transverse flux gradients and strand-to-strand coupling [24], [25].

4) Model Validation: The inductor configuration, shown in Fig. 1, was used to validate the proposed model. It consists of a random-wound winding on an electrical steel core. AC losses were computed assuming all turns were connected in series. The hybrid method couples the FEMM magnetostatic solver [26] with (1), and the results are compared with those obtained from the JMAG ac solver.

The analysis was performed for strand diameters ranging from 0.05 to 0.39 mm and for frequencies ranging from 50 to 10 kHz, at temperatures of 30, 70, and 297 K, assuming a current density of 20 A/mm^2 in an oxygen-free copper (OFCu,

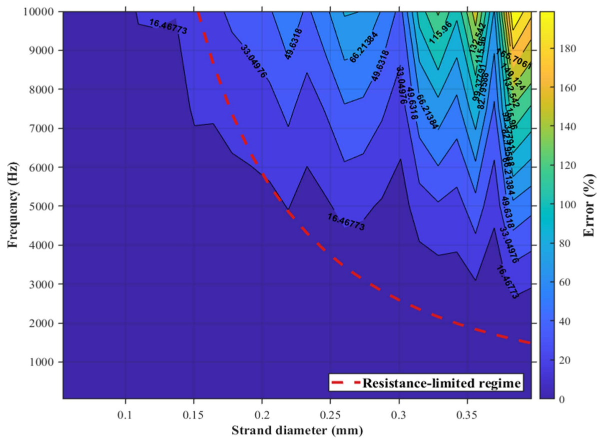

Fig. 2. Relative difference between analytical and FEM-calculated strand losses at 30 K (Hybrid-FEM comparison).

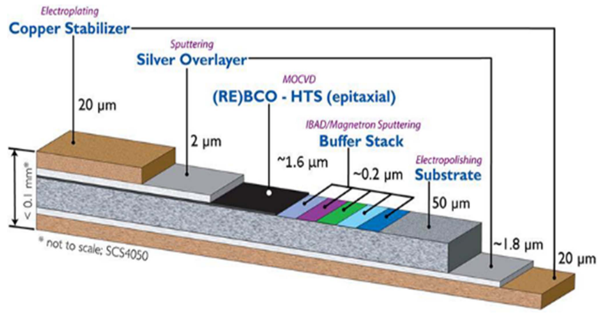

Fig. 3. Cross-section view of the REBCO coated conductor. (Reprinted from [29]).

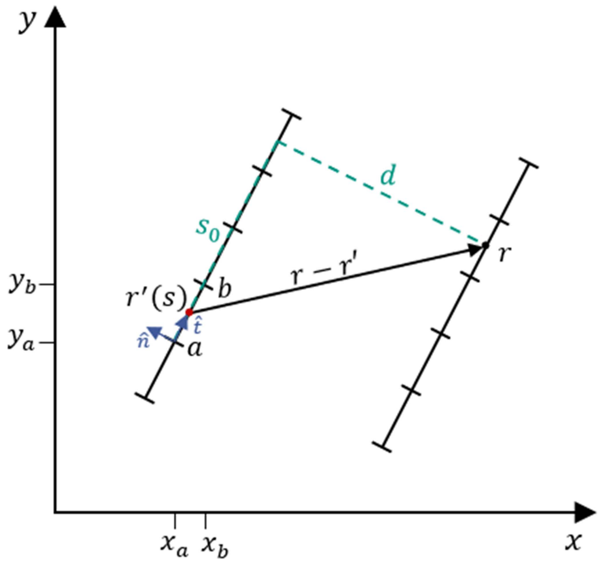

Fig. 4. One-dimensional line-segment discretization of HTS tapes.

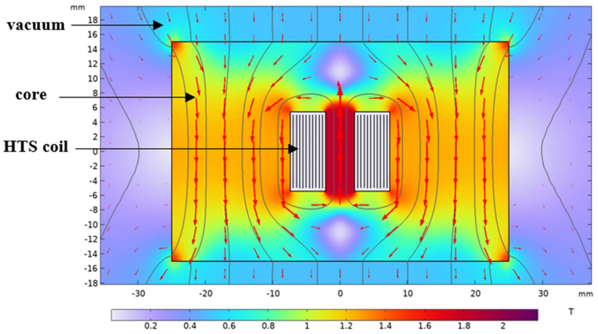

Fig. 5. Representative inductor configuration used for J-model validation, showing the magnetic flux density distribution for $I_n = 30\%$.

TABLE I
RELATIVE RMSE (%) BETWEEN THE DETAILED HYBRID MODEL AND THE JMAG AC SOLVER ACROSS TEMPERATURES

Temperature (K)	RMSE – Total (%)	RMSE – Resistance limited (%)
30	28.43	3.92
70	0.6187	0.6187
297	0.0045	0.0045

RRR100) conductor [9]. Fig. 2 shows the relative-error map between the hybrid model and the JMAG ac solver over the frequency–diameter plane. The analysis was also extended to a simplified model in which individual strands were not explicitly represented and an equivalent (homogenized) slot region was used instead of detailed strand placement. However, the strand locations and diameters were still considered when extracting the background magnetic field and computing the losses.

To quantify the model accuracy, we use the relative root-mean-square error (RMSE) defined as

$$\mathrm{RMSE} = \sqrt{\frac{1}{N}\sum_{i=1}^{N}\left(\frac{P_{\mathrm{Hyb},i} - P_{\mathrm{FEM},i}}{P_{\mathrm{FEM},i}}\right)^2} \tag{8}$$

where N is the number of calculation points, and $P_{\mathrm{Hyb},i}$and $P_{\mathrm{FEM},i}$are the losses from the hybrid model and the finite-element method (FEM) reference at point i, respectively. This RMSE is dimensionless. Since the deviations are squared, larger relative errors are penalized.

Table I shows that, at 30 K, the total RMSE is 28.43%, while the resistance-limited region is 3.92%. This difference indicates that many operating points at 30 K fall outside the resistance-limited regime (δ comparable or smaller than d_c). At 70 K and 297 K, the total and resistance-limited RMSE are identical (0.62% and 0.0045%), which implies that the full grid lies within the resistance-limited regime. The hybrid model then agrees very closely with JMAG.

The simplified model gives similar RMSE, indicating that homogenizing the strand region introduces negligible error while reducing the computation time by more than a factor of 10 compared with the ac solver.

B. Materials With Nonlinear Conductivity: HTS Tapes

In HTS coils with insulated tapes, two loss mechanisms are the main contributors under dynamic electromagnetic excitation. First, in the flux-creep regime ($J < J_c$), thermally activated vortex motion produces flux-creep dissipation [27] and hysteresis loss under time-varying fields or transport currents [11]. Second, eddy-current loss arises in the metallic stabilizer (Cu or Ag) bonded to the tape. Fig. 3 shows a representative of an HTS tape architecture.

1) Governing Equations (J-model): The electromagnetic behavior of REBCO tapes is modeled with a nonlinear current density J-based formulation derived from Maxwell's equations [13], [14], [15]. In 2-D (invariance along z-axis), the governing equations reduce to

$$-E_z(r,t) - \frac{\partial \phi(r,t)}{\partial z} - \dot{A}_{\text{ex}} = \int_S G(r,r')\left(\mu_0 \dot{J}_z(r',t) - \nabla^2 \dot{A}_{\text{ex}}(r',t)\right)\mathrm{d}^2 r' \tag{9}$$

where $r = (x,y)$ denotes the observation point and r' the source points integrated over S (superconducting region).

E_z is the axial electric field (V/m); Φ is the scalar electric potential (V); $\dot{A}_{\text{ex}}$ is the time derivative of the applied external magnetic vector potential (V·s/m); J_z is the axial current density (A/m^2); μ_0 is the permeability of free space (H/m).

$G(r,r')$ is the Green's function (fundamental solution) of Poisson's equation in the superconducting region S.

In 2-D,

$$G(r,r') = -\frac{1}{2\pi}\ln\|r-r'\|. \tag{10}$$

Within the HTS region, $\nabla^2 \dot{A}_{\text{ex}} = 0$ because the impressed source currents that generate A_{ex} is outside S.

The superconductor constitutive law follows the E-J power model [28]

$$E_z(r,t) = E_c\left|\frac{J_z(r,t)}{J_c(B(r,t),\theta(r,t))}\right|^{n(B,\theta)}\frac{J_z(r,t)}{|J_z(r,t)|}. \tag{11}$$

$J_c(B,\theta)$ and $n(B,\theta)$ are the field- and angle-dependent critical current density and power-law exponent, respectively, and E_c is the electric field criterion (typically 1×10^{-4} V/m in power applications).

We use the boundary element method (BEM) to discretize the problem. The current density in (11) is integrated only over the HTS region. Because HTS tapes have a high aspect ratio, we use a 1-D discretization along the tape width and neglect variation across the superconductor thickness.

Each discretized element of the tape is represented as a straight segment from $a = (x_a, y_a)$to $b = (x_b, y_b)$ as shown in Fig. 4.

With the arc-length parameter $s \in [0, L]$, where $L = \|b-a\|$ and $t = (b-a)/L$

$$r'(s) = a + s\cdot t, \quad s \in [0, L]. \tag{12}$$

$\hat{t}$ and $\hat{n} = [-t_y, t_x]$ are the local tangent and normal of the segment that contains the source point $r'(s)$.

Writing (10) in the local frame of the source segment, the Green function becomes

$$G(r,r') = -\frac{1}{2\pi}\ln\sqrt{(s_0-s)^2+d^2}. \tag{13}$$

With $s_0 = (r-a).\hat{t}, d = (r-a).\hat{n}$.

The discrete equation of (9) at an observation point i

$$\mu_0 t_{\text{sc}}\sum_{j=1}^{N_e} K_{ij}\dot{J}_j = -E_i - \dot{A}_{\text{ex},i} - \left.\frac{\partial\phi}{\partial z}\right|_i \tag{14}$$

where t_{sc} is the HTS layer thickness.

E_i is electric field at observation point r_i.

$\frac{\partial\phi}{\partial z}\big|_i$ is the transport current for the turn containing element i.

$K_{i,j}$ is an entry of the Green function matrix, it is the coefficient that quantifies the effect of source element j on observation point i, in the frame linked to the source element

$$K_{i,j} = -\frac{1}{2\pi}\int_0^L \ln\sqrt{(s_0-s)^2+d^2}ds$$

with the change variable $x = s_0 - s$ and the primitive

$$\int \ln\sqrt{x^2+d^2}dx = x\ln\sqrt{x^2+d^2} + d\tan^{-1}(x/d) - x$$

we obtain the closed form for $d \neq 0$

$$K_{i,j} = -\frac{1}{4\pi}\left(s_0\ln\left(s_0^2+d^2\right) - (s_0-L)\ln\left((s_0-L)^2+d^2\right) + 2d\left(\tan^{-1}\frac{s_0}{d} - \tan^{-1}\frac{s_0-L}{d}\right) - 2L\right).$$

For $d = 0$, when the observation and source are on the same tape line

$$K_{i,j} = -\frac{1}{2\pi}(s_0-L)(\ln|s_0-L|-1) - (s_0)(\ln|s_0|-1).$$

For multiturn coils, the gradient of the scalar electric potential ϕ is used to impose the transport current using a penalty feedback control [14], [15]

$$\frac{\partial\phi}{\partial z} = \gamma\boldsymbol{L}^T\left(\boldsymbol{I}_{\mathbf{app}}(t) - \boldsymbol{L}(\boldsymbol{a}.*\boldsymbol{J})\right). \tag{15}$$

$\boldsymbol{L}$ is a matrix that connect the per-turn current to each element. $\boldsymbol{L} \in \mathbb{R}^{N_t\times(N_t N_e)}$

$$L_{i,j} = \begin{cases}(-1)^{s_i}, & \text{if element } j \text{ belongs to turn } i,\\ 0, & \text{otherwise.}\end{cases}$$

s_i: current direction for coil/turn i (0 outward, out of page; 1 reverse, into page).

$\boldsymbol{a} = t_{\text{sc}}\boldsymbol{w}$ is the element surface vector.

$\boldsymbol{J}$: is the element current-density vector; $\boldsymbol{I}_{\mathbf{app}}$: is the per-turn current vector.

N_t: total number of turns; N_e: number of elements in each turn.

γ [V/ (A.m)]: regulation coefficient—if a turn current is too low, it adds a positive feedback field to increase it, and vice versa.

The rest of implementation is similar to [14] and [15]. The external magnetic vector potential A_{ex} is imported either from a FEM model or from a closed-form expression, and the current density is integrated using MATLAB's ode15 s.

The average ac power loss over a time period T_{elec} across all elements $N = N_t \times N_e$

$$P_{\text{avg}} = \frac{1}{T_{\text{elec}}}\int_0^{T_{\text{elec}}}\sum_{i=1}^{\boldsymbol{N}} a_i J_i(t).E_i(t)\,dt \tag{16}$$

with $E_i = E(J_i(t)),\ a_i = t_{\text{sc}}w_i$.

2) Assumptions and Limitations:

1) only hysteresis losses are accounted for in (9),
2) the HTS winding's self-field is counted twice in (9), which could cause discrepancies at high transport current.

Solution:

Use an external potential that removes the HTS self-field

$$A_{\text{ext}} = A_{\text{Full}} - A_{\text{HTS,Vac}}$$

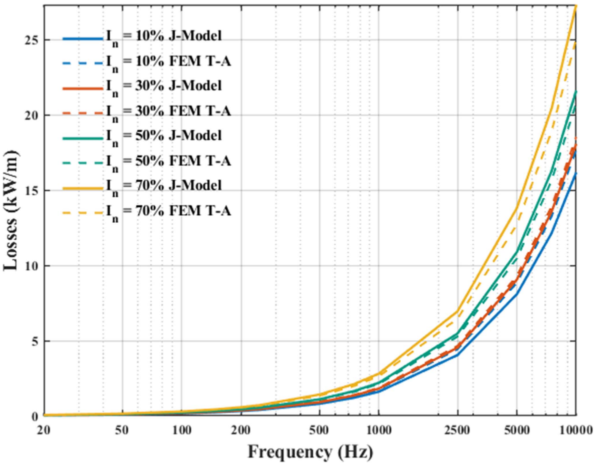

Fig. 6. AC losses in the HTS coils per active length (kW/m) as a function of frequency for $I_n = 10\%, 30\%, 50\%, 70\%$; J-model (solid) versus FEM(COMSOL) T–A (dashed).

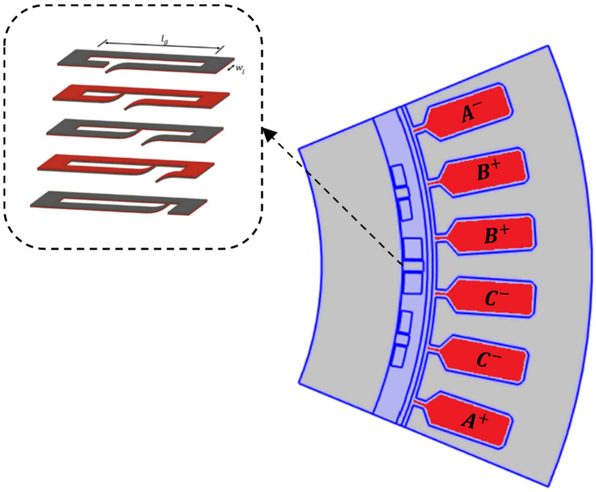

Fig. 7. Cross-section of the simulated topology and exploded view of the DUDA assembly.

where A_{Full} : background vector potential with all active parts excited, and $A_{\text{HTS,Vac}}$: background with only the HTS winding excited and all other domains set to vacuum.

3) Model Validation: To validate the proposed time-domain J-model for HTS tapes, an inductor consisting of ten turns per winding leg wound around a laminated electrical-steel core was analyzed at 70 K. An external alternating magnetic field $B_{\text{ext}} = B_0 \sin(2\omega t)\,\vec{y}$, with $B_0 = 1.5\ T$ and $\omega = 2\pi f$,and a sinusoidal transport current $I_{\text{app}} = I_0 \sin(\omega t)$ were applied. The frequency was varied from 20 Hz to 10 kHz, and the normalized current $I_n = I_0/I_c$ was set to 10%,30%, 50%, and 70% where $I_c = 500$ A and power-law index was $n = 29$. The REBCO tapes are 10 mm wide, 95 μm thick, with 400 μm inter-turn spacing (see Fig. 5).

The validation procedure comprised three steps.

1) *Reference solution:* Full 2-D finite-element simulations were performed in COMSOL Multiphysics using the T–A formulation [30].
2) *Input extraction:* From the COMSOL solution, the time-dependent external magnetic vector potential $A_{\text{ext}}(t)$ was exported at a set of scattered (x, y) sampling points for all time steps. These data were then interpolated in MATLAB onto the discrete spatial sampling points used by the J-model. For each winding leg, two sampling domains were defined on the left and right sides of the HTS stack, and the resulting waveforms were mapped directly to the tape discretization across the tape width.
3) *J-model computation:* The interpolated $A_{\text{ext}}(t)$ waveforms were used together with the imposed transport current as the input to the analytical J-model. The same temporal discretization was used consistently in the J-model computation. To avoid double counting of the HTS self-field, the self-field contribution was subtracted from the imported excitation before solving the time-domain model. The problem was solved over two periods, each sampled with 601 time steps.

Fig. 6 presents the ac loss per meter as a function of frequency for the four normalized current levels, comparing the J-model predictions against the COMSOL T–A reference. The agreement is good across the entire range.

At $I_n = 10\%$, the maximum relative error is 8.6% (at 20 Hz). At $I_n = 30\%$, the maximum error is 3.6%. At $I_n = 50\%$, the maximum error is 4.1%. At $I_n = 70\%$, the worst-case error is 9.0% (at 10 kHz).

Notably, losses at $I_n = 10\%$, and 30% are close, as they are primarily influenced by the strong external field of 1.5 T (dominated by magnetization losses). Over all the evaluated operating points, the worst-case deviation is below 10%, and in the other cases it is only a few percent. This level of agreement is acceptable for validation and enables fast parametric studies without running full FEM for every case. Moreover, the proposed model reduces computation time without compromising accuracy, achieving speedups of 10–20 times compared to COMSOL, depending on the problem geometry.

These results confirm that the J-model accurately reproduces both magnetization and transport loss contributions with high fidelity, making it suitable for subsequent machine-level loss mapping and system-level optimization studies.

III. IMPLEMENTATION IN ELECTRICAL MACHINE

A. Studied Topology

We investigate a 40-kW-class, 8-pole synchronous machine with a surface-mounted rotor formed by series-connected (soldered) REBCO HTS tapes assembled as a disk-up-down (DUDA) stack [29], [31], [32]. For each pole we use three DUDA stacks (see Fig. 7): one central stack and two side stacks, each one-third of the central thickness. The layout can be extended to 5- or 7-stack patterns around the pole to reduce the third-harmonic content of the air-gap flux. The stator uses a distributed winding, and VACODUR 49 is used for both stator and rotor laminations. Table II lists the machine parameters used in the simulations.

TABLE II
MACHINE PARAMETERS USED IN SIMULATION

Parameters	Symbol	Value	Unit
Stator outer radius	R_{so}	108.95	mm
Rotor outer radius	R_{ro}	77	mm
Airgap length	g	2.5	mm
Active length	L_a	100	mm
Central stack height	h_c	4	mm
Side stacks height	h_s	2.5	mm
No. of turns central stack	N_c	30	–
No. of turns per side stack	N_s	19	–
Number of slots	Q	48	–
Number of poles	$2p$	8	–
Rotor Current per layer	I_r	353.75	A
Stator current density (from [33])	J_s	40	A/mm^2

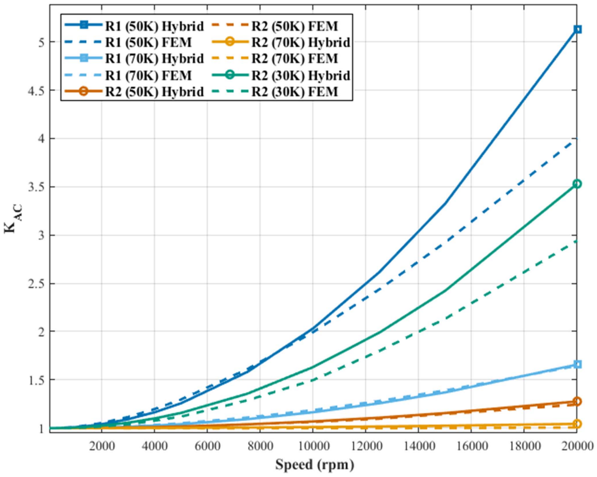

Fig. 8. Comparison of normalized ac loss coefficient K_{AC} between hybrid and FEM models for $R_1 = 0.1995$ mm and $R_2 = 0.0399$ mm.

B. Armature Winding With Stranded Conductors Litz Configuration

The armature winding was modeled using a Litz-wire configuration consisting of eight turns per slot and five strands per hand. A current density of 40 A/mm^2 was applied, and the hybrid model results were validated against JMAG simulations.

Two strand radii were selected for the study: $R_1 = 0.1995\ \mathrm{mm}$ and $R_2 = 0.0399\ \mathrm{mm}$, and a rotational speed range from 1 to 20 000 r/min. The simulations were performed using OFCu (RRR100) copper at cryogenic temperatures of 30, 50, and 70 K, with the corresponding conductivities taken from [9].

To compare the FEM and hybrid model results, a normalization coefficient was defined as

$$K_{\mathrm{AC}} = \frac{P_{\mathrm{speed}}}{P_{1\mathrm{r/min}}} \tag{17}$$

where P_{speed} and $P_{1\mathrm{r/min}}$ represent the total ac losses at a given speed and at 1 r/min, respectively. The results of the comparison are shown in Fig. 8.

Good agreement between the hybrid model and FEM is observed for both strand radii up to 14 000 r/min, with a maximum deviation $< 10\%$ across all temperatures. However, beyond this speed, the loss behavior depends on the strand radius and temperature. For at 50 K and 70 K, the winding remains in the resistance-limited regime and the hybrid model matches FEM up to 20 000 r/min. In contrast, for R_1 at 50 K and R_2 at 30 K, proximity effects become significant as shown in Fig. 9. The resulting magnetic screening drives a transition toward the inductive-limited regime, with proximity losses scaling down approximately as $\sqrt{f}$ [21]. As a consequence, the relative error increases, reaching 20% for R_2 at 30 K and 29% for R_1 at 50 K at 20 000 r/min.

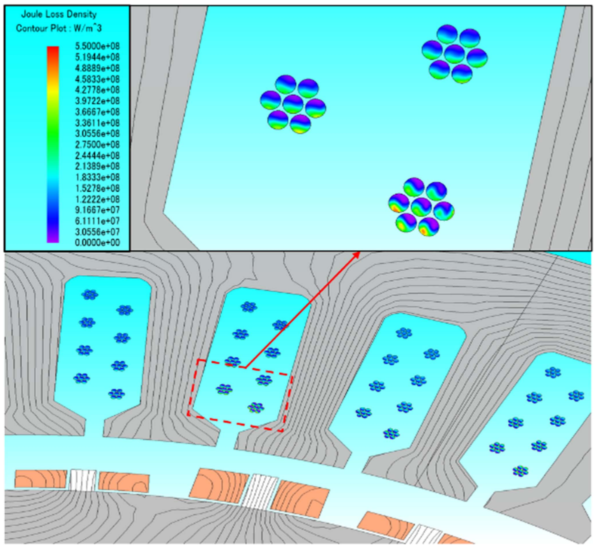

Fig. 9. Joule loss-density map—Litz winding (8 turns/slot, 5 strands/hand), R_1, 20 000 r/min, 50 K; proximity-effect losses dominate at this speed.

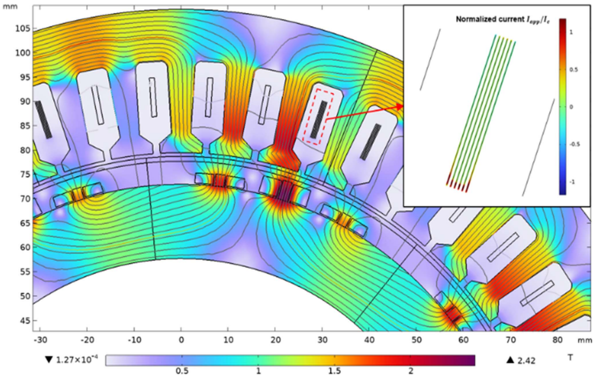

Fig. 10. Magnetic flux—density distribution—HTS armature winding at I_n = 10% and 4000 r/min; only phase A uses HTS tapes. Inset: normalized current distribution.

C. Armature Winding With HTS Tapes

As in the previous case, the armature winding uses HTS tapes. Six REBCO tapes [12] are modeled per slot and connected in series. Each tape has a width of 8 mm, a total thickness of 95 μm, an HTS layer thickness of 1 μm, and an inter-turn spacing of 120 μm (see Fig. 10).

The critical current and power exponent are fixed at $I_c = 1240$ A and $n = 24.23$, respectively. In the machine-level implementation, the external excitation $A_{\mathrm{ext}}(t)$ is extracted from the FEM solution and mapped to the HTS tape discretization using the same coupling procedure described in Section II-B-3. Since the rotor and stator windings are symmetric, we model a single

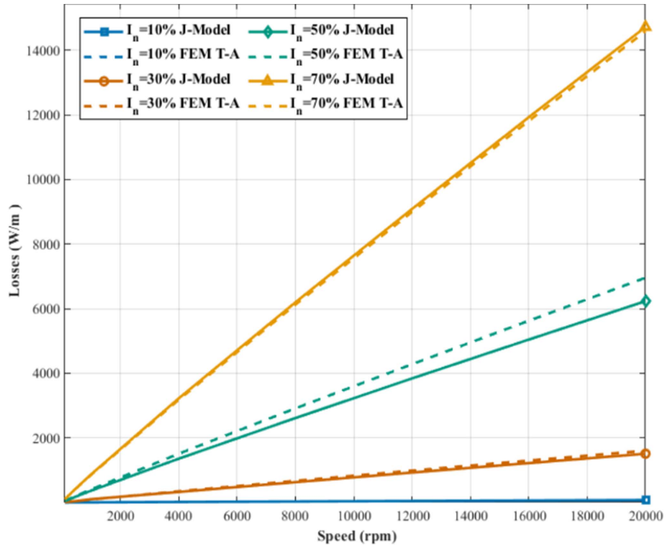

Fig. 11. Per-phase losses per active length (W/m) versus speed for $I_n = 10\%$, 30%, 50%, 70%; J-model (solid) versus FEM(COMSOL) T–A (dashed).

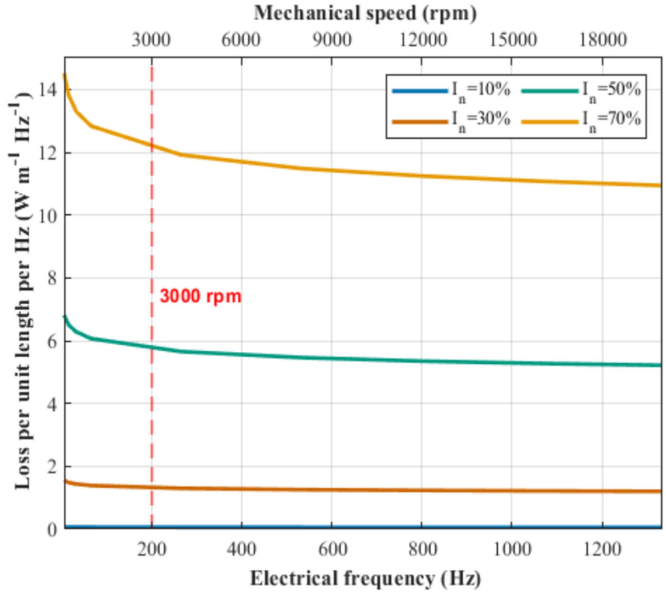

Fig. 12. Per-phase loss per active length per hertz (W m^{-1} Hz^{-1}) vs. electrical frequency.

phase and derive the total armature loss by multiplying by the number of phases.

Fig. 11 reports the losses (W/m) for phase A in the symmetry-reduced (only periodic-sector) model using both methods. The results agree across the entire speed range, with a maximum deviation of 10% at $I_n = 50\%$. The losses increase strongly with I_n, showing in this case they are mainly driven by transport current.

For fixed I_n, the loss per unit length per hertz—i.e., the loss per unit length divided by the fundamental electrical frequency—decreases with frequency (see Fig. 12). Using 100 r/min as the baseline, the drop is around 20% at 20 000 r/min and 11% at 3000 r/min; using 3000 r/min as the baseline, the drop at 20 000 r/min is ≈10%.

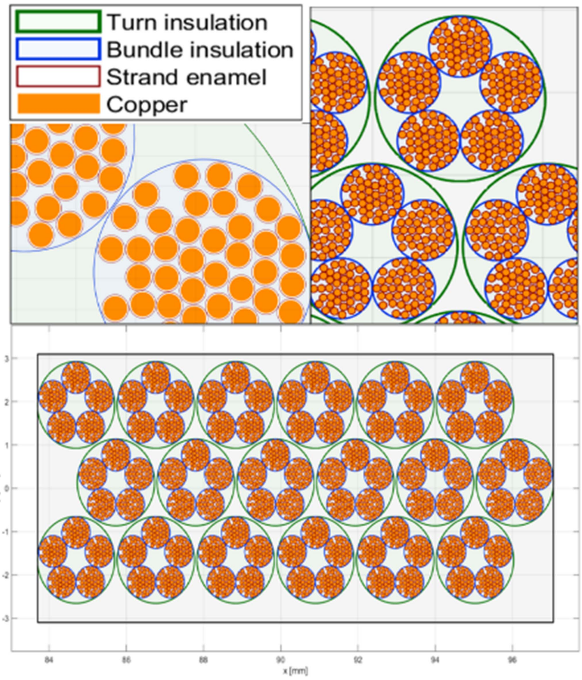

Fig. 13. Litz-wire arrangement on the net slot surface for the 18/5/43 configuration, showing strands, bundles, and turns insulation.

TABLE III
FIXED PARAMETERS FOR THE STUDY

Parameters	Symbol	Value	Unit
Ampere turns per slot	AT_{slot}	761	A.t
Number of parallel paths	a_p	8	–
Speed	N_{speed}	3000	rpm
Frequency	f	200	Hz

If a ∼10% error is acceptable, we can speed up the study by computing a single mid-speed (i_d, i_q) loss map and scaling with frequency. For better accuracy, we could solve at a few speeds across the range (anchor points) and interpolate the losses for the remaining speeds.

IV. LOSS ANALYSIS FOR DIFFERENT MATERIALS, NUMBER OF TURNS, AND TEMPERATURES

Using the topology of Section III-A, we evaluate the impact of conductor material**,** turn count per slot**,** and operating temperat**ure** on armature-winding losses. For an equivalent comparison, the same topology is used, and the same ampere-turns per slot are maintained across all variations. Table III lists the fixed parameters.

A. Litz-Wires Winding

1) Parameters: We consider normal-conducting materials—high-purity copper and aluminum [9], [10]—with different residual-resistivity ratios (RRR). For a fixed strand radius, the turns per slot are varied and a temperature sweep is performed to assess the loss behavior. Table IV summarizes the parameter variations used in this part.

TABLE IV
PARAMETER VARIATIONS OF THE LITZ-WIRE ARMATURE WINDING

Parameters	**Symbol**	**Value**	**Unit**
Residual resistance ratio	RRR	50, 10, 1000, 3000	–
Strand gauge	–	40	AWG
Number of turns	N_{turn}	18, 20, 24	–
Temperature	T	5–290	K

TABLE V
COPPER FILL FACTOR, TWIST FACTOR, AND PER-TURN CURRENT FOR THE SELECTED CONFIGURATIONS

Turns/bundles/strands	**Filling factor, k_{Cu}**	**T_f**	**I_{turn}(A)**
18/5/43	0.23	1.0807	42.2789
20/5/43	0.257	1.0880	38.0567
24/5/37	0.27	1.0759	31.7139

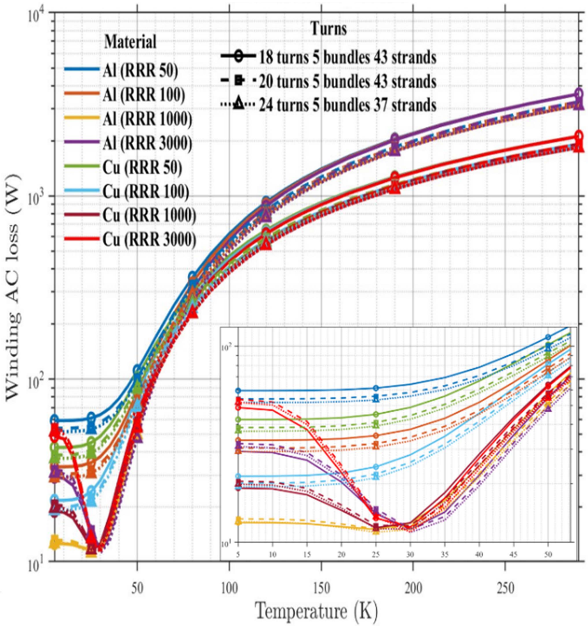

Fig. 14. Total winding ac loss versus temperature for Cu and Al conductors with different RRR values and turn configurations.

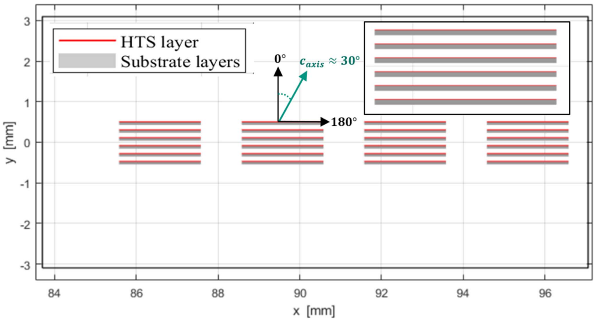

Fig. 15. HTS tape distribution for the 24 × 2 mm configuration within the net slot surface, with the HTS layer oriented toward the slot interior (winding centered around the slot axis).

2) Litz Winding Construction: The Litz winding is constructed using the guidelines in [8]. We first limit the strands per hand by

$$n_{\max} = 4\frac{\delta^2}{d_s^2} \tag{18}$$

and choose $N_{\text{SH}} < n_{\max}$. For all turns, we use five bundles per turn to reduce the skin effect at the turn level; the bundles are twisted about the center of each turn to equalize the flux-density gradient and the path length, thereby reducing circulating current.

Under $N_{\text{SH}} < n_{\max}$, the skin effect at the bundle level is reduced and transposition is sufficient to limit the circulating current. To account for the length increase due to Litz twisting, we include only two twist stages—bundle level and turn level—each modeled as a helix of pitch p_i and radius r_i (distance from the stage centroid to the strand or bundle center). The per-stage length factor is $k_i = \sqrt{1 + (2\pi r_i/p_i)^2}$ with $i = 1$ for the bundle level and $i = 2$ for the turn level.

Therefore, the twisted strand length is $L_{\text{twist}} = k_1 k_2 L_s$.

With all turns in series, each turn has N_{SH} strands per bundle and N_b bundles in parallel, so the number of parallel strand paths is $N_s = N_{\text{SH}} N_b$.

Since resistance is proportional to length, the per-strand resistance scales as $R_i = f_{12,i} R_{\text{DC}}$ with $f_{12,i} = k_1 k_2$ where R_{DC} is the untwisted resistance from (6). The equivalent turn resistance (parallel combination of strands) is

$$R_{\text{turn},t} = \left(\sum_{i=1}^{N_s} \frac{1}{R_i}\right)^{-1} = \frac{R_{\text{DC}}}{\sum_{i=1}^{N_s} \frac{1}{f_{12,i}}} \tag{19}$$

and the corresponding turn transposition factor is

$$T_f = \frac{1}{N_{\text{turn}}} \sum_{i=1}^{N_{\text{turn}}} F_{\text{turn},t} \tag{20}$$

which scales the resistance (and copper loss) to include the geometric increase in conductor length from bundle- and turn-level twisting.

Table V summarizes the copper fill factor $\boldsymbol{k_{Cu}}$, twist factor T_f, and per-turn current I_{turn} for each turns/bundles/strands configuration, evaluated for pitches $p_1 = 10 - 15$ mm and $p_2 = 25 - 30$ mm. Fig. 13 illustrates the Litz-wire configuration 18/5/43 as a representative example.

3) Results and Discussion: Fig. 14 shows total ac loss versus temperature. From room temperature down to approximately 100 K, Cu gives the lowest loss because skin effect dominates. As temperature decreases further, resistivity drops, skin loss diminishes, and the proximity effect becomes progressively stronger, producing a clear minimum near 30 K. Below this point, the loss increases driven by proximity-effect losses**,** especially for high-RRR conductors. For fixed ampere–turns per slot, increasing the turn count lowers current per strand and reduces loss over most of the range; however, below 30 K this benefit largely disappears—the higher strand count pushes proximity losses up, so higher turns become more lossy.

Across the cryogenic range (T<120 K), Al (RRR 1000) provides the lowest losses among the cases studied.

TABLE VI
GEOMETRICAL PARAMETERS OF THE HTS ARMATURE WINDING

Parameters	Symbol	Value	Unit
HTS tape thickness	t_{tape}	95	μm
HTS layer thickness	t_{sc}	1	μm
Inter-turn spacing	t_{gap}	120	μm

TABLE VII
HTS WIDTH–TURN–LAYER COMBINATIONS AND FILLING FACTOR

Turns per Slot	Layers	Tapes Width (mm)	k_{HTS}	I_{turn}(A)
5	1	8	0.095	152.22
6	1	8	0.116	126.85
10	2	4	0.095	76.11
12	2	4	0.116	63.42
20	4	2	0.095	38.05
24	4	2	0.116	31.71

TABLE VIII
POLYNOMIAL FITS FOR FRACTIONAL COP $\eta_{fc}(T_c)$ OF SINGLE-STAGE CRYOCOOLERS (PULSE-TUBE, STIRLING)

Cryocooler type	Coefficient of performance
Pulse tube	$\eta_{fc} = 1.0139.10^{-08} \times {T_c}^3 - 9.3879.10^{-06} \times {T_c}^2 + 1.9057.10^{-03} \times T_c$
Stirling	$\eta_{fc} = -3.5335.10^{-09} \times {T_c}^3 - 9.9354.10^{-06} \times {T_c}^2 + 3.2995.10^{-03} \times T_c$

TABLE IX
ELECTRICAL AND THERMAL CONSTRAINTS USED IN THE TORQUE–SPEED LOSS MAP OPTIMIZATION

Parameter	Symbol	Value	Unit
Maximum phase current	I_{max}	254	A
Maximum phase voltage	V_{max}	120	V
Maximum mechanical speed	N_{max}	5000	rpm
Cryocooler cooling capacity	$\dot{Q}_{c,cryocooler}$	70	W
Cold-tip temperature	T_c	50	K

B. *HTS Tapes Winding*

1) Parameters: In a study parallel to Section IV-A, we analyze HTS windings based on a commercial REBCO tape (Theva ProLine TPL4622-AP) [12]. The turns per slot and tape width are chosen to maintain similar slot utilization and ampere–turns per slot. The tape total thickness is $t_{\text{tape}} = 95\ \mu\text{m}$, the HTS layer thickness is $t_{\text{sc}} = 1\ \mu\text{m}$, the inter-turn spacing is $t_{\text{gap}} = 120\ \mu\text{m}$, and the interlayer spacing is set to half the tape width for each configuration. AC losses are computed over $T = 12.5$–80 K. Table VI summarizes the geometrical parameters of the HTS tapes [12].

Table VII lists the turn–width combinations and the tape filling factor $\boldsymbol{k}_{\mathbf{HTS}}$, defined as the ratio of the total tape cross-sectional area to the net slot area (inside the slot liner). Fig. 15 illustrates the HTS tape distribution for the 24×2 mm configuration as a representative example.

2) Characteristics: Using the HTS critical-current data in [12], the tape critical current is reported at the criterion $E_c = 10^{-4}$ V/m. Assuming the tape performance is homogeneous along its width and length, the corresponding critical current density $J_c(B,\theta)$ (or engineering current density $J_e(B,\theta)$) can be obtained directly from the measured $I_c(B,\theta)$. Fig. 16 shows that, at a given temperature, both J_c and the power-law exponent n depend on the magnetic-flux density B and its orientation θ. In HTS machines, the rotating field can reduce tape performance and increase ac losses; therefore, accurate loss calculation requires $J_c(B,\theta)$ and $n(B,\theta)$ for the winding slots.

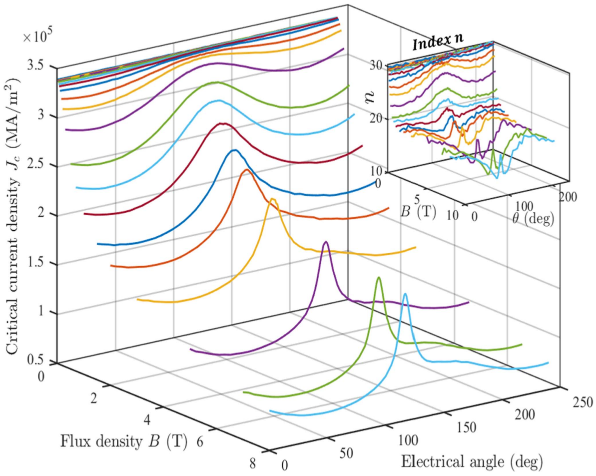

Fig. 16. Critical current density surface $J_c(B,\theta)$ for REBCO tape at 30 K as a function of magnetic flux density magnitude and orientation; inset: power-law exponent n(B,θ) [12].

a) Critical current for slot and phase: Each HTS tape is discretized into N_e elements across its width. For every element node, the incident magnetic flux density B and its local angle are rotated into the measurement frame [12]; the critical current density $J_c(B,\theta)$ and the $n(B,\theta)$ are then obtained by interpolation from the characterization data (see Fig. 16).

For tape j in layer ℓ, the instantaneous tape critical current is computed by integrating J_c across the tape width and multiplying by the superconducting layer thickness t_{sc}

$$I_{c,\ell j}\left(t\right) = t_{\text{sc}} \int_{\text{width}} J_c\left(s,t\right) ds. \tag{21}$$

The instantaneous slot critical current is the minimum over all the tapes of the slot

$$I_{c,\text{slot}}\left(t\right) = \min_{(\ell,j)} I_{c,\ell j}\left(t\right)$$

and the returned slot value is the minimum over one electrical period, which constitutes a conservative criterion

$$I_{c,\text{slot}_{\text{min}}} = \min_{t} I_{c,\text{slot}}\left(t\right). \tag{22}$$

For the phase, let a_p be the number of parallel paths of the winding. The instantaneous path critical current is

$$I_{c,\text{path } p}\left(t\right) = \min_{(\ell,j)\in\text{path}} I_{c,\ell j}\left(t\right) \tag{23}$$

and the phase critical current is obtained by summing the parallel paths and taking the period minimum

$$I_{c,\text{phase}}\ \left(t\right) = \min_{t} \sum_{p=1}^{a_p} I_{c,\text{path } p}\left(t\right). \tag{24}$$

b) Power-law exponent for slot and phase: We compute the exponent n in the E–J law $E = E_c\left|\frac{J}{J_c}\right|^n$ using the same rotated field and discretization at each time step.

For tape j in layer ℓ, the instantaneous width-weighted exponent is

$$n_{\ell j} = \frac{\int n\left(s,t\right) J_c\left(s,t\right) ds}{\int J_c\left(s,t\right) ds}. \tag{25}$$

Since tapes in a slot are connected in series. The total electric field per slot is

$$E_{\text{slot}}\ \left(I,t\right) = \sum_{\ell,j} E_{\ell,j}\left(I,t\right) = \sum_{\ell,j} E_c\left(\frac{I}{I_{c,\ell j}\left(t\right)}\right)^{n_{\ell,j}(t)}. \tag{26}$$

We define the instantaneous effective slot exponent as the log-log slope

$$n_{\text{slot}}\ \left(I,t\right) = \frac{d\ln E_{\text{slot}}\left(I,t\right)}{d\ln I} = \frac{I}{E_{\text{slot}}\left(I,t\right)}\frac{dE_{\text{slot}}\left(I,t\right)}{dI}. \tag{27}$$

Differentiating $E_{\text{slot}}(I,t)$ with respect to I and substituting into (27) gives

$$n_{\text{slot}}\ \left(I,t\right) = \frac{\sum_{\ell,j} n_{\ell,j}\left(t\right)\left(\frac{I}{I_{c,\ell j}(t)}\right)^{n_{\ell,j}(t)}}{\sum_{\ell,j}\left(\frac{I}{I_{c,\ell j}(t)}\right)^{n_{\ell,j}(t)}}. \tag{28}$$

If $t_{\min}$ is the time step at which the slot critical current is reached, $I_{c,\text{slot}_{\min}} = I_{c,\text{slot}}\ (t_{\min})$.

Then, the effective slot power-law index is

$$n_{\text{slot,eff}} = n_{\text{slot}}\left(I_{c,\text{slot}_{\min}}, t_{\min}\right). \tag{29}$$

Using symmetric topology and equal sharing across a_p parallel path. All paths have the same electric field. So, currents divide equally, $I_{\text{path}} = \frac{I_{\text{phase}}}{a_p}$

$$E_{\text{phase}}\ \left(I_{\text{phase}}, t\right) = E_{\text{path}}\left(\frac{I_{\text{phase}}}{a_p}, t\right).$$

Here, E_{path} and E_{phase} denote the total electric field, including the contributions from all stator slots that belong to a given parallel path and to a given phase, respectively.

Therefore,

$$n_{\text{phase}}\ \left(I_{\text{phase}}, t\right) = n_{\text{path}}\left(\frac{I_{\text{phase}}}{a_p}, t\right). \tag{30}$$

At the critical time step $t_{\min}$, with the phase critical current $I_{c,\text{phase}} = a_p\, I_{c,\text{path}}$ (equal sharing), the effective phase exponent is

$$n_{\text{phase,eff}} = n_{\text{path}}\left(\frac{I_{c,\text{phase}_{\min}}}{a_p}, t_{\min}\right). \tag{31}$$

3) Phase AC Resistance: We define the phase ac resistance as an effective resistance that depends on the normalized current I_n and the drive frequency f

$$R_{\text{phase,AC}}\left(I_n, f\right) = \frac{P_{\text{phase,avg}}\left(I_n, f\right)}{I^2_{\text{phase,rms}}} \tag{32}$$

where $P_{\text{phase,avg}}$ is the time-average over one electrical period T_{elec}.

4) Results and Discussion: We computed the armature-winding ac losses for all HTS configurations with the J-model; the phase normalized current $I_{n,\text{phase}}$ and the effective phase index $n_{\text{phase,eff}}$ are obtained from the measured $J_c(B,\theta)$ and $n(B,\theta)$ surfaces at each temperature (see Figs. 17 and 18).

From Fig. 17, $I_{n,\text{phase}}$ grows rapidly with temperature. For the same ampere-turns, the single-layer options (56 turns) show the lowest $I_{n,\text{phase}}$, especially at higher temperatures. This is consistent with the field distribution in the slot: in multilayer stacks, mutual fields modify the edge field, and layers nearer the slot opening (air-gap side) experience stronger transverse field. Both effects reduce I_c and thus increase $I_{n,\text{phase}}$. At low temperature (≈12.5–30 K), $I_{n,\text{phase}}$ is small for all options and the differences are minor.

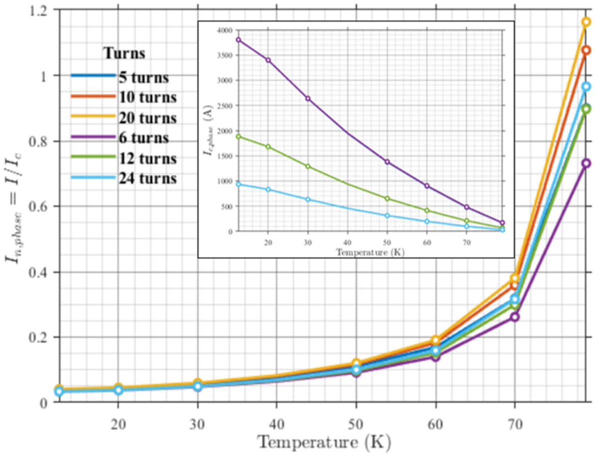

Fig. 17. Per-phase normalized current $I_n = I/I_c$ versus temperature for all turn configurations (see Table VII); inset: phase critical current I_c versus temperature.

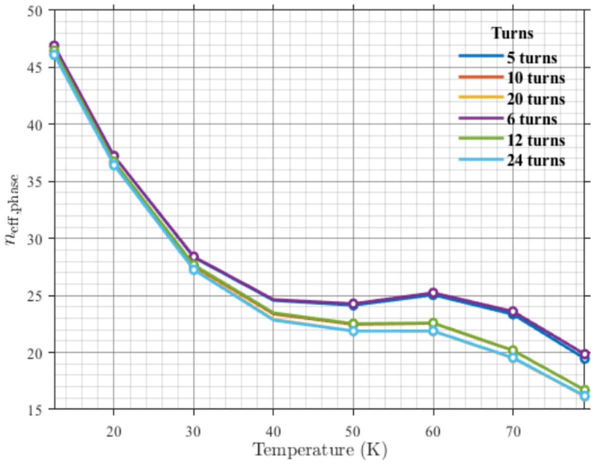

Fig. 18. Per-phase effective phase index $n_{\text{phase,eff}}$ versus temperature for all turn configurations.

Fig. 18 shows a similar trend for the effective phase index: It starts around 46 at 12.5 K and decreases with temperature, falling to 20–16 near 80 K, with higher turn counts having lower $n_{\text{phase,eff}}$.

Fig. 19 reports the winding ac losses. At low temperature, I_c is large so $I_n = I/I_c \ll 1$ and transport loss is negligible; total loss is set by magnetization in the local perpendicular field. Adding turns/layers places more tapes near the slot opening/bottom, where the perpendicular field $B_\perp$ is higher and less uniform (air-gap field plus neighboring tapes). Because small-amplitude magnetization loss scales as $\sim H^4_\perp$ [11], this nonuniformity dominates, so multilayer slots give higher loss than a single layer.

As temperature rises, I_c decreases and converges across the turn options. Thus I_n increases and transport loss—scaling as

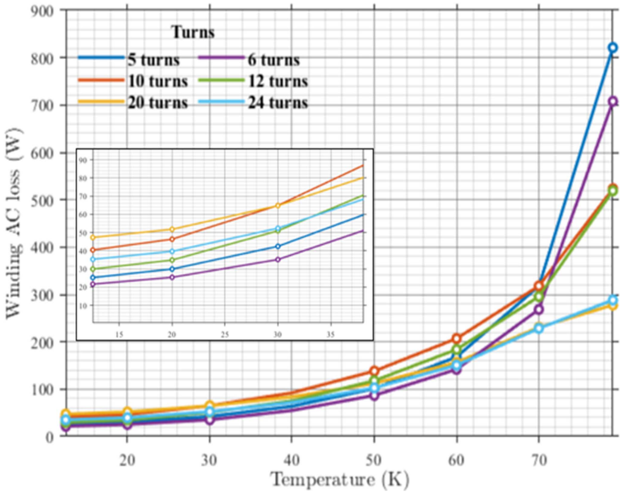

Fig. 19. Total winding ac loss versus temperature for all turn configurations.

$\sum I_{\text{tape}}^4/I_c^2$ for small–moderate I_n [11]—becomes important. With ampere-turns fixed, increasing the turn count reduces the current per turn; therefore I_n decreases with more turns and the transport loss drops. Between these limits there is a crossover (around 30 K for our topology): below this temperature, magnetization/proximity makes higher turn-count slots lossy; above it, transport losses favor higher turn-count.

We selected the 24-turn winding because, in the intended 40–70 K operating range, it delivers the lowest winding ac loss at fixed ampere–turns per slot.

C. Operating-Point and Cryocooler Selection

Based on Section IV-A and IV-B results, we select the operating cold-tip temperature T_c by evaluating feasible cryocoolers and their input power P_{input}. A candidate at T_c is feasible if its available cooling capacity exceeds the load

$$\dot{Q}_{\text{cap}}\left(T_c\right) > \dot{Q}_{\text{load}}\left(T_c\right) \tag{33}$$

and its required electrical input power is

$$P_{\text{input}}\ \left(T_c\right) = \frac{\dot{Q}_{\text{load}}\left(T_c\right)}{\text{COP}\left(T_c\right)} \tag{34}$$

The coefficient of performance is modeled as a fraction of the Carnot limit

$$\text{COP}\left(T_c\right) = \eta_{fc}\left(T_c\right)\text{COP}_{\text{Carnot}}\left(T_c, T_h\right) \tag{35}$$

$$\text{COP}_{\text{Carnot}}\ \left(T_c, T_h\right) = \frac{T_c}{T_h - T_c}. \tag{36}$$

With T_h the heat rejection temperature $T_h = 300\,\text{K}$.

The fractional efficiency $\eta_{fc}(T_c)$ reported in Table VIII is obtained from survey-based polynomial fits for a single-stage cryocooler, valid over the ranges 35–170 K for Pulse-tube and valid over 50–250K for Stirling as reported in [18].

Using Ladner's survey, the system mass M(kg) is estimated from the input power P_{input}.

Let $x = \log_{10}(P_{\text{input}}[W])$

$$\log_{10}\text{M} = c_3\ x^3 + c_2x^2 + c_1x + c_0$$

$$\left(c_3, c_2, c_1, c_0\right) = \left(–5.52610^{-9}, –5.56510^{-1}, –1.0931, 1.3315\right). \tag{37}$$

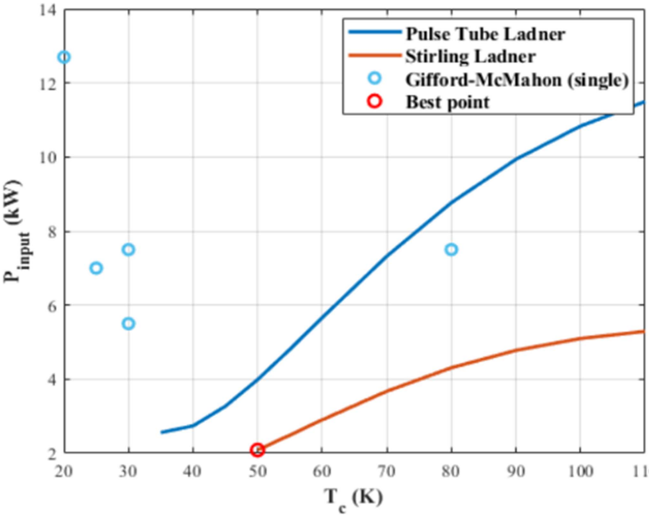

Fig. 20. Cryocooler input power versus cold-tip temperature T_c for Litz winding.

We then select the operating point and cooler that minimize $P_{\text{input}}(T_c)$ —or a weighted combination of input power and mass—among all feasible candidates within their survey or vendor-datasheet Tc limits [18], [19], [20]. (e.g., single stage Gifford–McMahon units).

In this study, the cryocooler sizing is intentionally based on the stator winding ac loss only. The stator winding is assumed to operate at cryogenic temperature, while the stator back iron remains near ambient temperature. Accordingly, Q_{load} in (33) is taken as the winding ac loss only. Stator-core losses and parasitic heat transfer from the warm stator structure to the cold winding are not included in this first-order sizing analysis. Therefore, the selected cryocooler should be interpreted as a lower-bound estimate of the winding cooling requirement. In a practical machine, these additional thermal loads must be included, and the slot geometry could be adapted to improve thermal isolation between the warm stator core and the cold winding, for example by allocating space for multilayer insulation or another thermal barrier.

For the cryocooler comparison, we adopt aluminum (RRR 1000), 24 turns, 5 bundles, and 37 strands for the Litz case, and the 24-turn, 2-mm configuration for the HTS armature. Using the corresponding AC-loss curves as functions of temperature, we evaluate several cryocooler families at each T_c: Pulse-Tube and Stirling coolers using survey-based fits, and single-stage Gifford–McMahon coolers using datasheet-based data. For each T_c, the required input power is computed from (34), and the mass is estimated using the survey correlation in (37). At a given T_c, the selected cryocooler is the feasible candidate that minimizes both input power and estimated mass.

Figs. 20 and 21 show a minimum at $T_c = 50$ K for Stirling cryocooler. For both windings, the highlighted points at 50 K satisfy capacity while delivering the lowest input power and mass.

Litz : Stirling cryocooler $\dot{Q}_{\text{cap}} = 51\ \text{W},\ P_{\text{input}} = 1.8\ \text{kW}$

HTS: Stirling cryocooler $\dot{Q}_{\text{cap}} = 105\ \text{W},\ P_{\text{input}} = 3.67\ \text{kW}$.

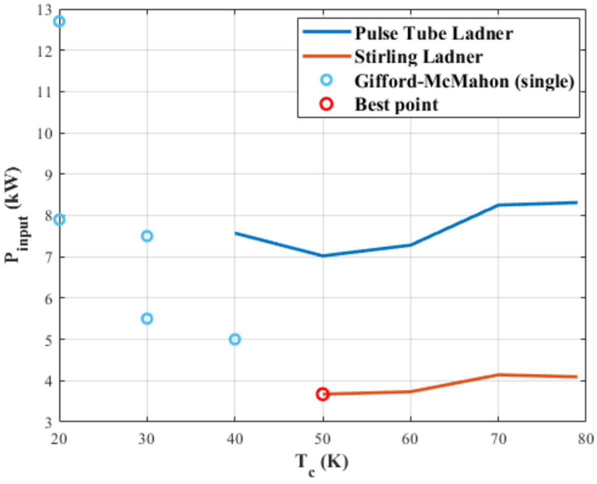

Fig. 21. Cryocooler input power versus cold-tip temperature T_c for HTS winding.

We therefore adopt $T_c = 50$ K as the operating temperature for both designs, cooled by a single-stage Stirling cryocooler.

V. Armature Winding Loss Maps

A. Armature Winding D-Q Loss Maps at 3000 R/Min

At $T_c = 50$ K, we compare the selected winding options: (a) Litz wire (Al, RRR 1000), 24 turns, 5 bundles, 37 strands (AWG-40); and (b) HTS winding, 24 turns of 2-mm REBCO tape arranged in four layers.

Geometry and electrical data follow Tables II and III. The inverter limits are $V_{\max} = 120$ V and $I_{\max} = 254$ A, and the rotor excitation is held constant (no field control).

Loss maps are computed on a 13 × 13 grid in the *d*–*q* plane with $i_d, i_q \in [-I_{\max}, +I_{\max}]$. For each grid point, we sample half of the electrical period using half-wave symmetry for three-phase sinusoidal current excitation: 64 magnetostatic solutions in FEMM are computed over $[0\, T_{\text{elec}}/2]$ and the full-period response is then reconstructed. The resulting fields feed the winding-loss models, and losses are averaged over the period. Figs. 22 and 23 present the winding-loss distributions at 3000 r/min for the Litz and HTS configurations, respectively. Within the inverter current limit $I_{\max} = 254$ A, the peak loss is about 50 W for the Litz winding and 80 W for the HTS winding.

For the Litz case, the iso-loss contours are nearly circular and d/q symmetric, indicating that loss scales primarily with current magnitude $\|\mathrm{i}_{dq}\| = \sqrt{i_d^2 + i_q^2}$ rather than phase angle. At 3000 r/min with AWG-40 strands, losses are skin-effect dominated; proximity effects are small because of the 2.5 mm air gap and the steel return path attenuate rotor-field and interslot coupling.

In contrast, the HTS map shows elliptical iso-loss contours. Losses clearly depend on the current phase.

At this speed, the innermost contour is below 10 W. Representative operating points are as

$$(i_d, i_q) = \ (0195)\ A \rightarrow \text{Loss} = 38\text{W}$$

$$(i_d, i_q) = \ (-195, 0)\ A \rightarrow \text{Loss} = 35.7\text{W}$$

$$(i_d, i_q) = \ (195, 0)\ A \rightarrow \text{Loss} = 17\text{W}.$$

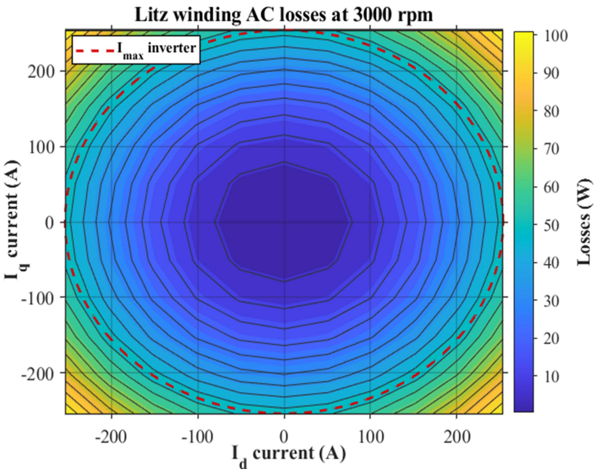

Fig. 22. Litz winding AC-loss distribution in the *d*–*q* current plane at 3000 r/min ($T_c = 50$ K).

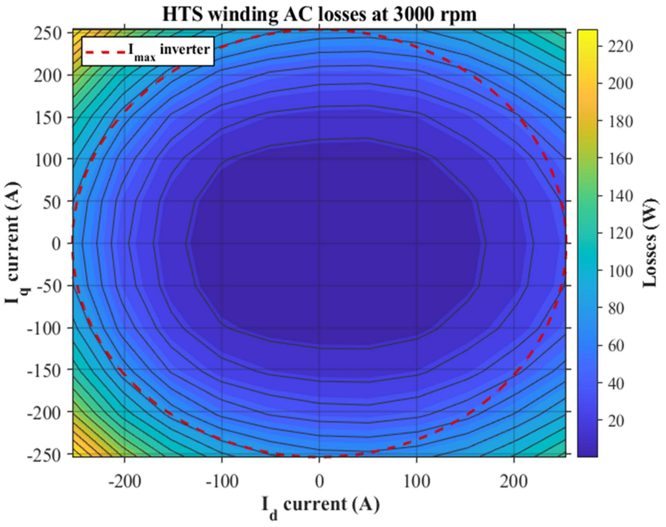

Fig. 23. HTS winding AC-loss distribution in the *d*–*q* current plane at 3000 r/min ($T_c = 50$ K).

This behavior originates from the angular dependence $J_c(B, \theta)$. The tapes wide face(width) is nearly parallel to the radial field B_r, so the penalizing component is the field normal to the tapes, which is approximately the tangential component B_θ, $B_\perp \approx |B_\theta|$.

1) The torque-producing current i_q adds a tangential armature reaction field, increasing $|B_\theta|$ and thus $B_\perp \rightarrow J_c$ decreases locally → loss increases.
2) At $i_q = 0$, negative i_d (field-weakening) reduces B_r ; the air-gap field redistributes and the flux near the slot opening bends more tangentially, raising B_θ and $B_\perp \rightarrow$ loss increases.
3) Positive i_d (magnetizing current) strengthens B_r and tilts the total field vector more radially, aligning it closer to the wide face of the tape, thereby reducing $B_\perp \rightarrow J_c$ increases → loss decreases.

B. Armature Winding AC Loss Maps in the Speed-Torque Plane

To evaluate the armature winding AC losses over the operating torque–speed range, an efficiency-oriented optimization is performed. For each operating point $(N_{\text{speed}}, T_{\text{req}})$, the stator currents are selected to minimize the total motor losses while satisfying inverter and cryocooler capacity limits.

At each operating point, the problem is formulated as

$$\min_{i_d, i_q} P_{\text{loss}}\left(i_d, i_q, N_{\text{speed}}\right)$$

Subject to

$$\begin{cases} \sqrt{v_d^2 + v_q^2} < V_{\max}, \\ \sqrt{i_d^2 + i_q^2} < I_{\max}, \\ T\left(i_d, i_q, N_{\text{speed}}\right) = T_{\text{req}}\ . \\ P_{\text{AC,Stator winding}} < \dot{Q}_{c,\text{cryocooler}} \end{cases}$$

Here, i_d and i_q are the *d*–*q* axis current components, v_d and v_q are the corresponding voltage components, T denotes the electromagnetic torque, and P_{loss} represents the total motor losses at the given operating point. The feasible torque–speed envelope $(N_{\text{speed}}, T_{\text{req}})$, is first determined by sweeping the mechanical speed from $N_{\text{speed}} = 1\ \text{r/min}$ to $N_{\max} = 5000\ \text{r/min}$ in steps of 25 r/min using a similar optimization procedure. Based on this envelope, the above optimization is then solved at each point of a 30 × 30 grid in the torque–speed plane. For each grid point, characterized by the mechanical speed N_{speed} and required torque T_{req}, the optimizer returns the current pair (i_d, i_q) that minimizes the total motor losses while respecting the voltage, current, and cryocooler constraints.

The main limits used in the optimization are summarized in the Table IX.

Figs. 24 and 25 show the armature-winding ac losses in the speed–torque plane for the Litz-wire and HTS-tape configurations, respectively, while Fig. 26 shows the normalized current I_n of the HTS winding.

C. Discussion and Analysis

1) Torque–Speed Envelope and Loss Trends: Base speed is defined as the highest speed on the optimized torque–speed envelope at which the required torque can be achieved without field weakening, i.e., before negative i_d is required to satisfy the inverter voltage limit under the imposed current and cryocooler constraints. With this definition, the HTS armature exhibits a lower base speed than the Litz reference case (2481 r/min versus 3615 r/min), corresponding to a 31% reduction relative to the Litz case. In the field-weakening region, the HTS winding also sustains a lower peak torque, consistent with its higher ac losses in this operating range. The additional losses increase the effective phase ac resistance R_{ac}, leading to a larger resistive voltage drop. Under the inverter voltage limit, this reduces the voltage margin available for the back-EMF and inductive terms, thereby limiting the current and, consequently, the achievable torque. At the maximum speed of 5000 r/min, the Litz winding delivers 88.5 N·m, compared with 57.8 N·m for the HTS winding, corresponding to an approximate 35% torque reduction

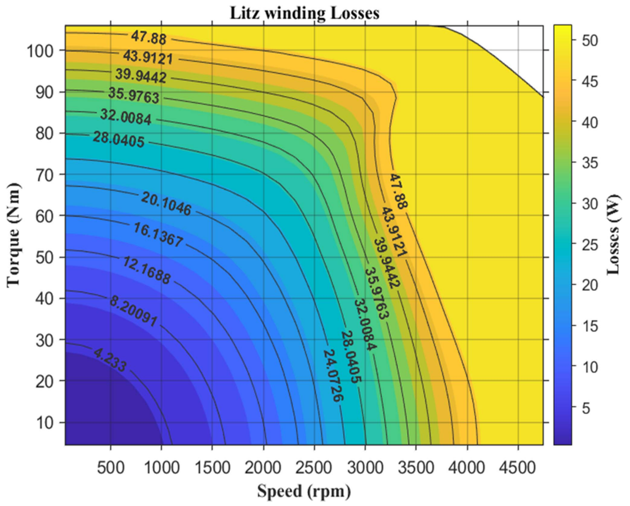

Fig. 24. Litz armature winding AC losses in the speed–torque plane at $T_c = 50$ K.

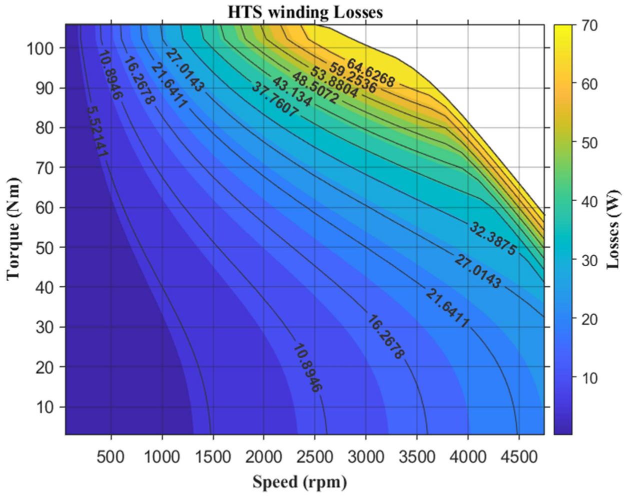

Fig. 25. HTS armature winding AC losses in the speed–torque plane at $T_c = 50$ K.

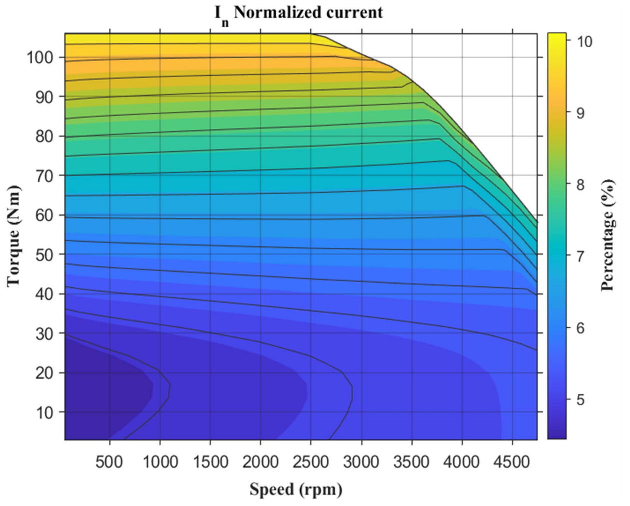

Fig. 26. Normalized current I_n of the HTS armature winding in the speed–torque plane at $T_c = 50$ K.

relative to the Litz case. In addition, the maximum mechanical power obtained within the optimized operating envelope is 27.5 kW for the HTS armature and 40 kW for the Litz armature.

2) MTPA Region (Below Base Speed):

1) *Litz winding:* the loss scales primarily with current magnitude $\|i_{dq}\|$ (skin-effect dominated).
2) *HTS winding:* the loss shows stronger dependence on electrical frequency than on the normalized current I_n. In the MTPA region at high torque, I_n is kept at approximately 10%, however $(T, N_{\text{speed}}) = (105\ \text{N}\cdot\text{m},\ 200\ \text{r/min})$ the loss is 5.8 W, whereas at $(T, N_{\text{speed}}) = (105\ \text{N}\cdot\text{m},\ 2481\ \text{r/min})$ the loss is 68 W.

3) Field-Weakening (Above Base Speed):

1) *Litz winding:* behavior remains skin-effect dominated, and proximity-effect contributions are weak. The optimizer selects a strongly negative i_d in this region, even at low torque, to increase the motor efficiency. In this operating range, steel losses dominate the total losses (around 560 W at maximum speed); therefore, a negative i_d is injected to reduce the incident field in the stator and, consequently, the steel losses, at the expense of an increased stator current. Reducing the rotor field in the stator also decreases proximity-effect losses originating from the rotor. Since the maximum winding losses (∼52 W) remain below the cryocooler capacity $\dot{Q}_{c,\text{cryocooler}}$, the winding losses do not constrain the overall loss optimization.
2) *HTS winding:* loss is driven mainly by the normalized current I_n [see I_n map Fig. 26] rather than by speed. In this region, the ac resistance significantly influences the terminal voltage, and a strong negative i_d both permits an extension of the operating speed range and helps reduce the steel losses; however, as discussed in Section V-A, it also increases the losses in the HTS winding.

4) Controlled Rotor Excitation: With controlled rotor excitation, the air-gap flux in the field-weakening region can be reduced, which decreases the required negative i_d and lowers the winding losses, especially for the HTS winding, since this topology exhibits a clear loss penalty for strongly negative i_d in field-weakening. However, the control of this excitation is constrained by the thermal stability of the HTS rotor: rapid modulation of the field current induces significant ac losses within the superconducting tape, forcing dynamic flux regulation to be restricted to slow transients to prevent quenching. As a result, fast torque control must be provided solely by the stator armature current especially for rotor winding with a high turns count.

5) Design and Operating Regimes: HTS armature windings typically exhibit a smaller tape-to-slot fill factor (see Table VII), which improves coolant access and can permit more tapes to be packed into the same slot, thereby increasing the potential power density. For ac operation, it is generally recommended to keep the normalized current $I_n \leq 10\%$ in order to maintain manageable HTS losses. Subject to the cryocooler power budget, the number of tapes in the slots can be increased with only a small, tolerable increase in I_n. This favors HTS windings for applications that require high torque at medium speeds, whereas for very-high-speed operation, a Litz armature winding is the preferred choice.

6) Air Core Machine: An air-core topology, particularly in the stator, can reduce the dominant loss components in the machine and thereby lower the losses in the HTS tapes, especially in the field-weakening region. However, using a topology that removes electrical steel from the teeth and/or back iron may reduce the motor performance, primarily the torque capability, and may also modify the flux path in a way that increases the incident field on the HTS tapes. A dedicated study should therefore be performed to determine the best compromise between a fully iron-cored design and a partially iron-cored or air-core machine, depending on the performance requirements.

VI. CONCLUSION

This article presented a unified and validated framework for predicting armature-winding ac losses in electrical machines using either Litz conductors or REBCO HTS tapes. The framework combined a fast hybrid model for Litz windings, including skin and proximity effects with turn- and bundle-level transposition, with a time-domain J-model for HTS windings based on measured $J_c(B, \theta)$ and $n(B, \theta)$ data. Both approaches were validated against finite-element simulations and then applied to machine-level loss analysis, cryocooler selection, and operating-map generation under inverter and thermal constraints. The results showed that incorporating cryocooler capacity as a hard constraint in the torque–speed optimization can significantly reduce the feasible operating envelope of the HTS armature beyond what inverter limits alone would impose.

The comparison further showed that the preferred armature technology is strongly operating-region dependent. In the MTPA region, the HTS armature can provide lower winding loss at a given torque when operated at low normalized current and favorable field orientation. In the field-weakening region, however, the Litz armature becomes preferable because its loss remains primarily skin-effect dominated, whereas the HTS winding experiences a stronger loss penalty as negative i_d increases the magnetic-field component normal to the tape surface and raises the effective ac resistance. Consequently, the HTS armature exhibits a reduced feasible operating envelope relative to the Litz reference case, including a lower base speed and lower torque capability at maximum speed.

The main design implication is that armature-winding selection should not be based on conductor technology alone, but also on the intended speed–torque duty, admissible normalized current, and available cooling capacity. For applications emphasizing medium-speed, high-torque operation, HTS armatures remain attractive provided the normalized current remains low and adequate cryogenic support is available. For very-high-speed operation and extended field weakening, Litz armatures are generally the more robust choice.

Future work will investigate controlled rotor excitation as a means of reducing the required negative i_d and the associated HTS loss penalty, quantify the influence of PWM-induced current harmonics on ac losses in both winding types under inverter-driven conditions, study scaling to higher power levels, and extend the comparison to full duty-cycle efficiency evaluation.

APPENDIX A
BREAKDOWN OF LOSS COMPONENTS IN LITZ WINDING

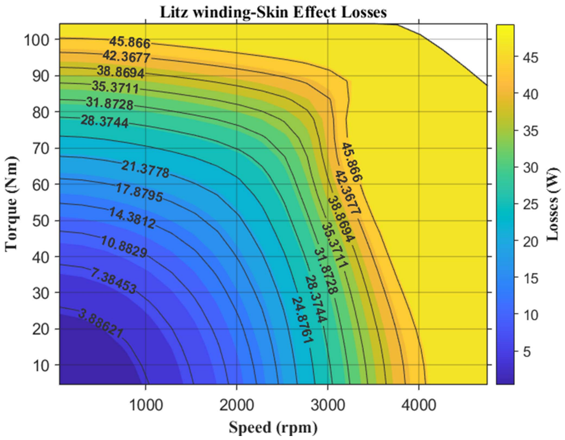

Fig. 27. Litz armature winding: Skin effect losses in the speed–torque plane at $T_c = 50$ K.

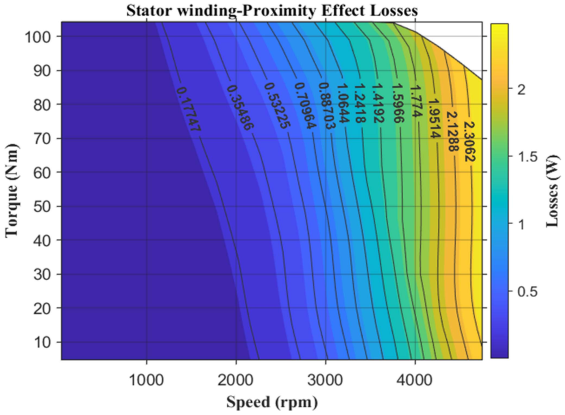

Fig. 28. Litz armature winding: Proximity effect losses in the speed–torque plane at $T_c = 50$ K.

APPENDIX B
COMPARISON OF ARMATURE-WINDING AC LOSSES IN HTS AND LITZ CONFIGURATIONS

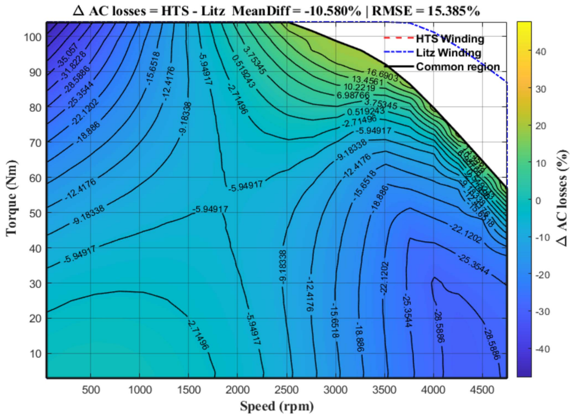

Fig. 29. Difference in armature winding ac losses between Litz and HTS in the speed–torque plane at $T_c = 50$ K.

REFERENCES

[1] K. S. Haran et al., “High power density superconducting rotating machines—Development status and technology roadmap,” *Supercond. Sci. Technol.*, vol. 30, no. 12, Nov. 2017, Art. no. 123002.

[2] T. F. Tallerico, J. J. Scheidler, D. Lee, and K. S. Haran, “Electromagnetic redesign of NASA’s high efficiency megawatt motor,” in *Proc. AIAA Propulsion Energy 2020 Forum*, 2020, pp. 1–15.

[3] M. Zhang et al., “AC loss estimation of HTS armature windings for electric machines,” *IEEE Trans. Appl. Supercond.*, vol. 23, no. 3, Jun. 2013, Art. no. 5900604.

[4] J. A. Ferreira, “Improved analytical modeling of conductive losses in magnetic components,” *IEEE Trans. Power Electron.*, vol. 9, no. 1, pp. 127–131, Jan. 1994.

[5] C. R. Sullivan, “Computationally efficient winding loss calculation with multiple windings, arbitrary waveforms, and two-dimensional or three-dimensional field geometry,” *IEEE Trans. Power Electron.*, vol. 16, no. 1, pp. 142–150, Jan. 2001.

[6] A. Bardalai, X. Zhang, T. Zou, D. Gerada, J. Li, and C. Gerada, “Comparative analysis of AC losses with round magnet wire and Litz wire winding of a high-speed PM machine,” in *Proc. 22nd Int. Conf. Elect. Machines Syst.*, Aug. 2019, pp. 1–5.

[7] C. R. Sullivan, “Optimal choice for number of strands in a Litz-wire transformer winding,” *IEEE Trans. Power Electron.*, vol. 14, no. 2, pp. 283–291, Mar. 1999.

[8] C. R. Sullivan and R. Y. Zhang, “Simplified design method for Litz wire,” in *Proc. IEEE Appl. Power Electron. Conf. Expo.*, Mar. 2014, pp. 2667–2674.

[9] N. J. Simon, E. S. Drexler, and R. P. Reed, “Properties of copper and copper alloys at cryogenic temperatures,” NIST Monogr. 177, National Institute of Standards and Technology, Gaithersburg, MD, USA, Feb. 1992.

[10] P. D. Desai, H. M. James, and C. Y. Ho, “Electrical resistivity of aluminum and manganese,” *J. Phys. Chem. Reference Data*, vol. 13, no. 4, pp. 1131–1172, 1984.

[11] E. H. Brandt and M. Indenbom, “Type-II-superconductor strip with current in a perpendicular magnetic field,” *Phys. Rev. B*, vol. 48, no. 17, pp. 12893–12906, 1993.

[12] S. C. Wimbush and N. M. Strickland, “A public database of high-temperature superconductor critical current data,” *IEEE Trans. Appl. Supercond.*, vol. 27, no. 4, Jun. 2017, Art. no. 8000105.

[13] E. H. Brandt, “Superconductors of finite thickness in a perpendicular magnetic field: Strips and slabs,” *Phys. Rev. B*, vol. 54, no. 6, pp. 4246–4264, Aug. 1996.

[14] S. Otten and F. Grilli, “Simple and fast method for computing induced currents in superconductors using freely available solvers for ordinary differential equations,” *IEEE Trans. Appl. Supercond.*, vol. 29, no. 8, Dec. 2019, Art. no. 8202008.

[15] C. C. T. Chow, F. Grilli, and K. T. Chau, “Numerical modelling of HTS tapes under arbitrary external field and transport current via integral method: Review and application to electrical machines,” *Supercond. Sci. Technol.*, vol. 34, no. 11, Oct. 2021, Art. no. 113002.

[16] JMAG, *JMAG-Designer (Electromagnetic Field Analysis Software)*, JSOL Corporation, 2025. [Online]. Available: https://www.jmag-international.com

[17] COMSOL, *COMSOL Multiphysics Reference Manual*, COMSOL AB, 2024. [Online]. Available: https://www.comsol.com/comsol-multiphysics

[18] D. R. Ladner, “Performance and mass vs. operating temperature for pulse tube and Stirling cryocoolers,” Cryocoolers 16, in *Proc. Int. Cryocooler Conf.*, 2011, pp. 633–644.

[19] Bluefors, “Gifford-McMahon (GM) cryocoolers — AL series,” Bluefors Cryocooler Product Overview, 2025. [Online]. Available: https://bluefors.com/products/cryocoolers

[20] Sumitomo Heavy Industries Cryogenics, “Cryocooler Product Catalogue,” SHI Cryocoolers, 2023. [Online]. Available: https://www.shicryogenics.com/

[21] T. J. E. Miller, “Design of brushless permanent-magnet machines,” Motor Design Book LLC, USA, 2010.

[22] T. El Hajji, S. Hlioui, F. Louf, M. Gabsi, G. Mermaz-Rollet, and M. Belhadi, “Hybrid model for AC losses in high-speed PMSM for arbitrary flux density waveforms,” in *Proc. Int. Conf. Elect. Mach.*, Aug. 2020, pp. 2426–2432.

[23] J. A. Ferreira, “Appropriate modelling of conductive losses in the design of magnetic components,” in *Proc. 21st Annu. IEEE Conf. Power Electron. Specialists*, 1990, pp. 780–785.

[24] P. B. Reddy, T. M. Jahns, and T. P. Bohn, “Transposition effects on bundle proximity losses in high-speed PM machines,” in *Proc. IEEE Energy Convers. Congr. Expo.*, 2009, pp. 1919–1926.

[25] C. R. Sullivan and R. Y. Zhang, “Analytical model for effects of twisting on Litz-wire losses,” in *Proc. IEEE Appl. Power Electron. Conf. Expo.*, Mar. 2015, pp. 1222–1229.

[26] D. Meeker, “FEMM 4.2 User’s manual,” Finite Element Method Magnetics, 2015. [Online]. Available: https://www.femm.info/wiki/manual

[27] Y. B. Kim, C. F. Hempstead, and A. R. Strnad, “Flux creep in hard superconductors,” *Phys. Rev.*, vol. 131, no. 6, pp. 2486–2495, Sep. 1963,.

[28] J. Rhyner, “Magnetic properties and AC losses of superconductors with power law current–voltage characteristics,” *Physica C, Supercond.*, vol. 212, no. 3–4, pp. 292–300, Dec. 1993.

[29] THEVA, “Products,” 2026. [Online]. Available: https://www.theva.com/products

[30] F. Huber, W. Song, M. Zhang, and F. Grilli, “The T–A formulation: An efficient approach to model the macroscopic electromagnetic behaviour of HTS coated conductor applications,” *Supercond. Sci. Technol.*, vol. 30, no. 3, Jan. 2017, Art. no. 034003.

[31] T. Arndt et al., “New coil configurations with 2G-HTS and benefits for applications,” *Supercond. Sci. Technol.*, vol. 34, no. 9, Sep. 2021, Art. no. 095006.

[32] R. A. H. de Oliveira, O. Taalibi, and T. Arndt, “Compact HTS motor designs especially useful to be cooled by liquid hydrogen,” *IEEE Trans. Appl. Supercond.*, vol. 34, no. 6, Sep. 2024, Art. no. 5203305.

[33] F. Marignetti, S. Carbone, and V. Delli, “Cryogenic characterization of copper-wound linear tubular actuators,” *IEEE Trans. Ind. Electron.*, vol. 57, no. 1, pp. 312–320, Jan. 2010.